PHOTONICS Research

# Frequency stabilization and tuning of breathing solitons in $Si_3N_4$ microresonators

Shuai Wan,[1,2,†] Rui Niu,[1,2,†] Zheng-Yu Wang,[1,2] Jin-Lan Peng,[3] Ming Li,[1,2] Jin Li,[1,2] Guang-Can Guo,[1,2] Chang-Ling Zou,[1,2,4] and Chun-Hua Dong[1,2,*]

[1]CAS Key Laboratory of Quantum Information, University of Science and Technology of China, Hefei 230026, China
[2]CAS Center for Excellence in Quantum Information and Quantum Physics, University of Science and Technology of China, Hefei 230026, China
[3]Center for Micro and Nanoscale Research and Fabrication, University of Science and Technology of China, Chinese Academy of Sciences, Hefei 230026, China
[4]e-mail: clzou321@ustc.edu.cn
*Corresponding author: chunhua@ustc.edu.cn

Received 14 May 2020; revised 11 June 2020; accepted 19 June 2020; posted 22 June 2020 (Doc. ID 397619); published 21 July 2020

**Dissipative Kerr solitons offer broadband coherent and low-noise frequency combs and stable temporal pulse trains, having shown great potential applications in spectroscopy, communications, and metrology. Breathing solitons are a particular kind of dissipative Kerr soliton in which the pulse duration and peak intensity show periodic oscillation. Here we have investigated the breathing dissipative Kerr solitons in silicon nitride ($Si_3N_4$) microrings, while the breathing period shows uncertainties of around megahertz (MHz) order in both simulation and experiments. This instability is the main obstacle for future applications. By applying a modulated signal to the pump laser, the breathing frequency can be injection locked to the modulation frequency and tuned over tens of MHz with frequency noise significantly suppressed. Our demonstration offers an alternative knob for the control of soliton dynamics in microresonators and paves a new avenue towards practical applications of breathing solitons.** 

https://doi.org/10.1364/PRJ.397619

## 1. INTRODUCTION

Optical solitons that maintain their localized structures during propagation can be generated by balancing dispersion and nonlinearity in the propagation media [1,2]. This phenomenon was first demonstrated in optical fiber, aiming to transmit information with increased bandwidth [3]. Since then, these kinds of localized pulses have been explored and realized in various nonlinear systems and enable a variety of scientific and technological applications [4–8]. Whispering gallery mode (WGM) microresonators, which have the advantages of high optical quality factor ($Q$ factor) and small mode volume [9], could greatly enhance light–matter interaction and thus provide an alternative platform for studying this fascinating nonlinear physics [5,6,10–15]. In addition, the microresonator in the integrated photonic platform is excellent for future applications with high stability, reduced size, and lower costs.

The first observation of an optical microcomb was realized in 2007 [16], and after several years of deep studies in overcoming the challenges of low coherence, an optical soliton was successfully generated in a crystalline microresonator [10]. Compared to the aforementioned soliton generation schemes, in addition to the balance of dispersion and nonlinearity, soliton generation in WGM microresonators also requires the balance of loss and gain. Such optical soliton is called a dissipative Kerr soliton (DKS) and was first observed in the mode-locked fiber laser [17]. Different from the mode-locked fiber laser, where the gain is from an active medium, the gain in the passive WGM microresonator is the parametric gain of four-wave mixing (FWM) stimulated by an external continuous-wave (CW) laser. The rapid development of DKSs in microresonators makes them quite a good candidate for applications in ultrahigh-data-rate communication [18], quantum key distribution [19], high-precision optical ranging [20,21], dual-comb spectroscopy [22,23], low-noise microwave sources [24,25], optical clocks [26], and astronomical spectrometer calibration [27,28].

Associated with DKS, a series of novel nonlinear phenomena have been observed, such as dark pulses, Cherenkov radiation, Raman self-frequency shift, and breathing solitons [6,29–37]. In particular, breathing solitons exhibit periodic oscillation behavior in both amplitude and pulse duration, which is related to the Fermi–Pasta–Ulam recurrence [31]. It has drawn a lot of attention for fundamental studies of nonlinear physics and was recently demonstrated in experiments [31–37]. It was revealed that the breathing soliton state could exist in the detuning region between the modulation instability state and the stable DKS state because of intrinsic dynamical instability [31–35] or in the conventionally stationary DKS region

because of intermode interaction like avoided mode crossing [36]. Furthermore, in addition to bright breathing solitons, dark breathing solitons have also been observed in normal dispersion microresonators [37]. However, in the aforementioned studies, only the basic features of the breathing behavior are reported, and the breathing soliton is treated as an unwanted state because of the degradation of soliton stability. Currently, there are only few works addressing control of the breathing soliton [38,39]. One work [38] numerically investigated an intrinsic injection locking of breathing frequency to the repetition rate of the same soliton state, but the requirement is too stringent to be implemented in current microresonator systems. Another work [39] focused on the multiple sidebands of comb lines generated by a strongly modulated pump laser with external radio frequency (RF) signal to increase the spectroscopy resolution. Therefore, the stability or noise properties of the breathing soliton still need to be carefully studied.

In this work, we demonstrate the stabilization and control of the breathing frequency of the breathing soliton via injection locking. Through both numerical and experimental studies, we demonstrate that the breathing frequency can be injection locked by applying an appropriate modulation signal to the pump laser, and then the phase noise of the system is remarkably suppressed. Different from Ref. [39], the modulated signal is applied after the formation of the initial breathing soliton, and the characterization of the breathing feature and the suppressed noise of the modulated breathing soliton is performed in our study. Furthermore, the stabilized breathing frequency is tuned over 50 MHz. Our approach to stabilize and control the breathing frequency paves the way towards the applications of the breathing soliton. For example, the breathing soliton provides a robust way to transfer RF frequencies between very different optical frequency lines through the broadband soliton spectrum. Additionally, our demonstration also provides a convenient approach to study the differential absorption spectra by comparing the sidebands of each comb line due to the locked breathing frequency modulation.

## 2. DEVICE FABRICATION AND SETUP OF SOLITON GENERATION

For frequency comb generation, which requires anomalous group velocity dispersion, the $Si_3N_4$ integrated microring resonator with a cross section of 800 nm × 1800 nm and a diameter of 200 μm is fabricated from a silicon substrate wafer with 500 μm silicon and 3 μm wet oxidation silicon dioxide ($SiO_2$). The first step is to grow the stoichiometric $Si_3N_4$ film of 800 nm thickness with no cracks. Since cracks by high tensile stress typically start from the edge of the wafer and propagate into the center area, a diamond scribe is used to create some trenches around the wafer to avoid the cracks [40], and then the total 800 nm $Si_3N_4$ is deposited by using low-pressure chemical vapor deposition (LPCVD) at 770°C in steps of approximately 400 nm thickness. In order to remove residual N–H bonds in the $Si_3N_4$ film, high-temperature annealing at 1100°C in nitrogen atmosphere for 5 h is performed after each deposition step [40–42]. After the deposition, the wafer is diced into pieces, and the device is then patterned by using e-beam lithography with hydrogen-silsesquioxane (HSQ) resist (FOx–16 from Dow Corning). Following the development of the pattern, the film is etched with a $CHF_3/O_2$-based gas in an inductively coupled plasma (ICP) etcher. After removing the residual resist with a buffered oxide etch (BOE), the $Si_3N_4$ film on the backside of the substrate is also etched to keep a balance of tensile stress between the front side and back side of the substrate [43,44]. To further reduce the absorption loss, the substrate is again annealed under the aforementioned conditions for 4 h. Finally, an upper cladding of 3 μm $SiO_2$ is deposited by using plasma-enhanced chemical vapor deposition (PECVD) to protect the sample.

Figure 1(a) shows the scanning electron microscopy (SEM) picture of a typical device, which consists of a microring and a straight bus waveguide. The SEM picture of the microring cross section before removing the residual photoresist is shown in the upper right inset, with the corresponding fundamental optical mode profile shown in the bottom inset. The setup of our experiment is shown in Fig. 1(b). A tunable CW laser (Toptica CTL 1550) is coupled into and out of the chip through lensed fibers. The coupling loss of lensed fibers is measured to be ~3.5 dB at each facet. In the inset of Fig. 1(c), a typical transmission spectrum of a fundamental mode is shown and fitted by a loaded $Q$ factor of ~$1.5 \times 10^6$. The high extinction ratio of the resonance indicates a high intrinsic $Q$ factor of $3 \times 10^6$ and high efficiency energy delivering from the bus waveguide to the modes; both are beneficial for nonlinear optical effects. The wavelength division multiplexer (WDM) with the bandwidth

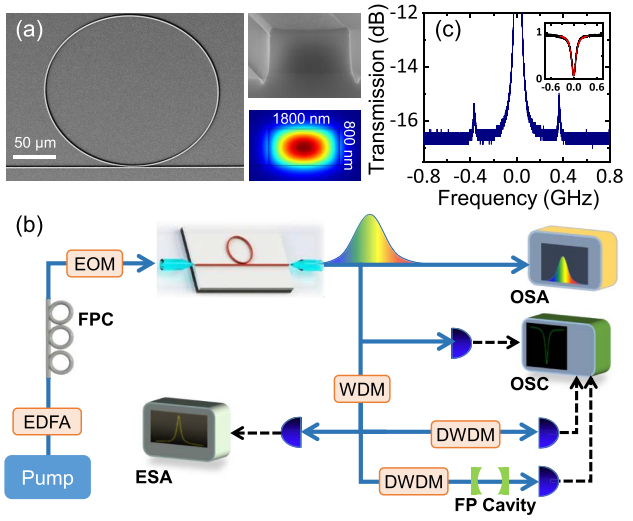


**Fig. 1.** (a) Scanning electron micrographs of a $Si_3N_4$ microring with diameter of 200 μm. Insets show the microring cross section of 1.8 μm × 0.8 μm and the corresponding fundamental transverse-magnetic mode profile. (b) Experimental setup for Kerr frequency comb generation. EDFA, FPC, EOM, WDM, DWDM, FP, OSC, and ESA are erbium-doped fiber amplifier, fiber polarization controller, electro-optical modulator, wavelength-division multiplexer, dense wavelength-division multiplexer, Fabry–Perot cavity, oscilloscope, and electronic spectrum analyzer, respectively. (c) Detailed comb line spectrum of a breathing soliton measured by the FP spectrum analyzer, with two sidebands indicating the breathing frequency around 0.4 GHz. The inset shows a typical resonance of the microring, with a loaded $Q$ of $1.5 \times 10^6$ according to the Lorentzian fitting (red line).

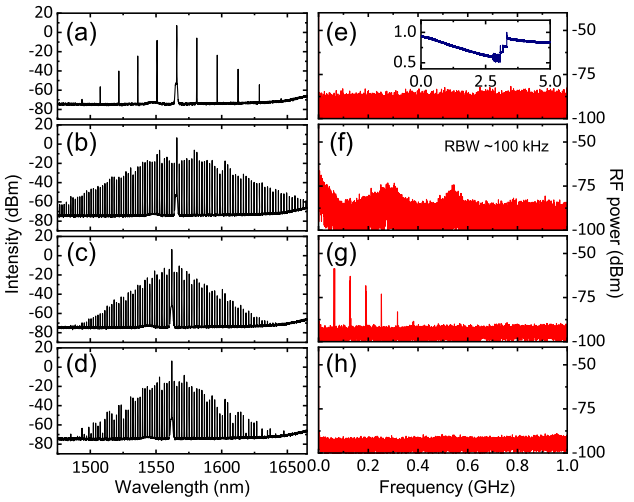


**Fig. 2.** Evolution of the soliton generation processes during the scanning of the pump laser detuning. (a)–(d) Typical optical spectra. Four evolution stages are (a) primary comb, (b) modulation instability comb, (c) breathing soliton, and (d) stable soliton, respectively. (e)–(h) The corresponding evolution of RF spectra. Inset: the transmission spectrum of the microring when the laser frequency is scanned across the resonance mode.

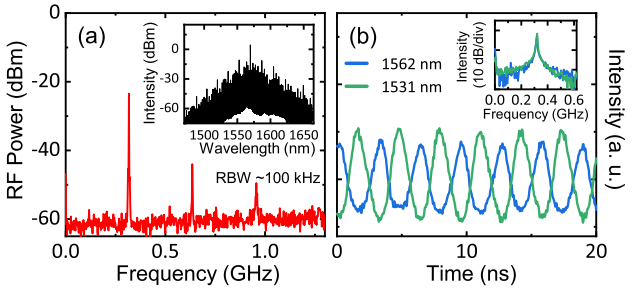


**Fig. 3.** Features of a breathing soliton. (a) The detailed RF spectrum of a breathing soliton state. Inset: the corresponding optical spectrum. (b) The recorded fast power evolution of a single comb line around the center (1562 nm, blue curve) and in the wings (1531 nm, green curve) of the optical spectrum of a breathing soliton. Inset: the corresponding Fourier transform spectrum.

of 20 nm is used to filter out several comb lines to obtain the low-frequency RF spectrum, and the dense wavelength division multiplexer (DWDM) with the bandwidth of 2 nm is used to filter out a single comb line to detect the power evolution at difference frequency. The Fabry–Perot cavity with the free spectral range (FSR) of 1.5 GHz, combined with the DWDM, is used to acquire the breathing sidebands of the specific comb line.

Soliton generation is achieved by sweeping the pump laser frequency over a resonance mode with on-chip power of 100 mW from the blue-detuned regime to the red-detuned regime [1,11,18,23]. During the laser frequency scanning, the cavity fields build up, and a strong nonlinear four-wave mixing effect induces the comb generation and essentially realizes the soliton. A complete spectral evolution can be divided into four stages, including a primary comb, a modulation instability (MI) comb, a breathing soliton, and a stable soliton, as shown by the optical spectra and RF spectra in Fig. 2. The inset is the corresponding transmission spectrum when scanning the pump. By carefully monitoring the transmitted power and stopping the pump frequency scanning at certain detuning points, four stages can be accessed in the experiment.

## 3. RESULTS AND DISCUSSION

### A. Breathing Soliton

Among the four stages of comb evolution, we are particularly interested in the breathing soliton. We verified the generation of breathing solitons in different devices with varying pump conditions. Figure 1(c) shows the optical spectrum measured by a Fabry–Perot cavity spectrometer. Two sidebands are obvious around the comb line, showing a breathing frequency $f_{br}$ of about 380 MHz. In another device, we studied the RF spectrum and temporal oscillation of individual comb lines as shown in Fig. 3. The breathing soliton is in a multisoliton state. From the RF spectrum, we can find that the breathing frequency is around 320 MHz. Then the DWDM is used to filter out the single comb line around the center (1562 nm) and the wings (1531 nm), which is detected by a fast photodetector (PD) and recorded by an oscilloscope as shown in Fig. 3(b). Here we record the traces over 200 ns and compute the RF spectrum based on the Fourier transform. As shown in the inset of Fig. 3(b), the oscillation frequency is the same as the frequency shown in Fig. 3(a), and the traces of the two comb lines are nearly out of phase when compared with each other, revealing that there exists a periodic energy exchange between comb lines around the center and the wings, which is a characteristic of Fermi–Pasta–Ulam recurrence and a typical signature of breathing solitons.

Comparing the breathing solitons in different experiments, we found that the breathing behavior could be robustly obtained in our devices, while its frequency varies from device to device. Even for a single device, the breathing frequency is not fixed. Here we observe that the linewidth of the RF beatnote is on the order of megahertz, indicating a fast drifting of the breathing frequency. In the time traces, the fluctuations are obvious even in a 10 ns time scale. Therefore, the problems of the inhomogeneous breathing frequencies and the frequency instability hinder the potential applications of the breathing soliton.

### B. Scheme of Injection Locking

The stabilization and control of the breathing frequency is of great significance, because it is not only helpful for a better understanding of nonlinear dynamics in microresonators but also critical for many potential applications. Here we envision two intriguing application scenarios enabled by breathing solitons. First, we could use a single breathing soliton, instead of stable solitons in the dual-comb scheme, for applications in spectroscopy. As can be noted from Fig. 1(c), with the occurrence of the breathing soliton, a series of sidebands can be observed around each comb line. Compared with the mode spacing of each comb line, these sidebands have much smaller frequency separation, which is equal to the breathing frequency. Therefore, the generated sidebands can provide additional differential absorption spectra around each comb line, and

an enhanced local resolution is expected. Second, the breathing could transfer a sub-gigahertz (GHz) signal among all comb lines that would span an octave of wavelength. Thus, the breathing soliton could be used for distributing RF frequency references.

Nevertheless, from our experiments, for the same chip, the breathing frequency depends on the pump power and the pump detuning, which can be affected by environmental fluctuations, such as the chip temperature, the polarization drift in the fiber, and the coupling between the lensed fiber and the chip. It is almost impossible to suppress all these imperfections in the experiments. Therefore, we propose to lock the breathing frequency by an external injection of RF signal as illustrated in the inset of Fig. 4(c). An intensity electro-optic modulator (EOM) was introduced to modulate the pump power with an appropriate modulation signal. The frequency sidebands generated by the modulator could stimulate the four-wave mixing in a single mode and expand mode to mode during soliton generation. This stimulated process competes with the natural oscillation induced by spontaneous four-wave mixing in breathing solitons. We expect it dominates the sidebands' generation with strong enough modulation depth, the wide oscillation spectrum caused by a spontaneous process, and the environmental fluctuation being suppressed.

In order to investigate the feasibility of this approach, the numerical simulation is performed based on the coupled-mode equation (CME) [45–47]. First of all, we numerically test the stages of frequency comb generation with fixed pump power of 100 mW. The simulation parameters of the microring are the same as the device used in our experiments. Figure 4(a) shows the simulated evolution of the intracavity power when we scanned the pump frequency. For more details about the numerical model, see Appendix A. In good agreement with our experiments (Fig. 2), there are clearly four states as the laser is tuning across the resonance mode [6]. By stopping the laser frequency on the breathing soliton stage, it can be observed that the intracavity power experiences periodic oscillation as shown in the inset of Fig. 4(a). A spectral envelope evolution of the breathing soliton is also depicted in Fig. 4(b), which shows that the power of the breathing soliton flows to the wings of the spectrum and returns to the center periodically; this agrees with Fig. 3(b). Then the injection-locking scheme is numerically investigated by applying a modulation signal on the pump power with a modulation frequency $f_{\mathrm{mod}}$, which is close to $f_{\mathrm{br}}$. Figure 4(c) shows the RF spectra for the breathing soliton with and without injection locking. It is found that the breathing frequency is locked to the $f_{\mathrm{mod}} = 270$ MHz (red line) even though it is about 17 MHz away from its natural breathing frequency (287 MHz, blue line). In addition, the linewidth of the beatnote is much narrower than it would have been without injection locking.

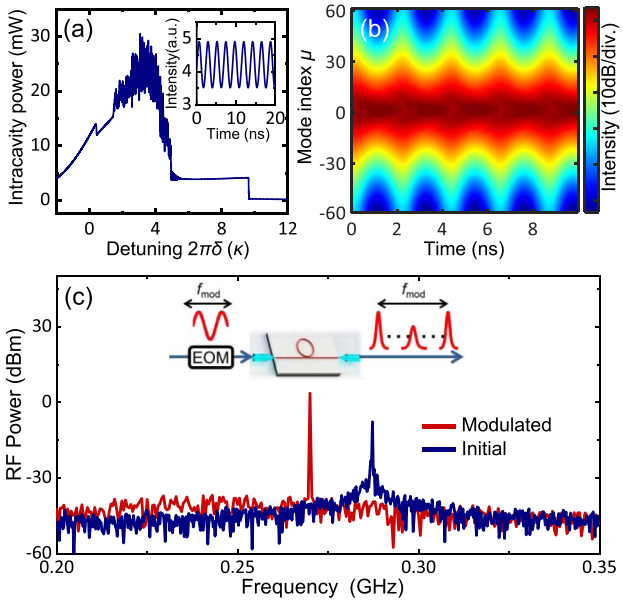


**Fig. 4.** (a) Simulated evolution of the intracavity power when the laser frequency is scanned across the resonance mode. The inset shows the oscillations of the power for a fixed laser frequency in the breathing soliton state. (b) Periodic spectrum evolution of a breathing soliton state. (c) RF spectra of the initial breathing soliton state (blue line) and modulated breathing soliton state (red line). The initial breathing frequency $f_{\mathrm{br}}$ is 287 MHz, and the modulated frequency $f_{\mathrm{mod}}$ is 270 MHz. The inset shows the concept of injection locking of a breathing soliton. A modulation signal with $f_{\mathrm{mod}}$ is applied to the pump laser after the appearance of breathing soliton, and $f_{\mathrm{br}}$ is injection locked if $f_{\mathrm{mod}}$ is within the locking range.

### C. Stabilization of the Breathing Frequency

With the scheme validated numerically, we performed injection locking for the breathing frequency stabilization. In our experiment, we use a sinusoidal wave signal to drive the EOM and monitor the evolution of the RF spectrum around the initial $f_{\mathrm{br}}$ when the modulation power varies from −50 dBm to −5 dBm with frequency of 281 MHz. The experimental results are summarized in Fig. 5. Before we turn on the modulator,

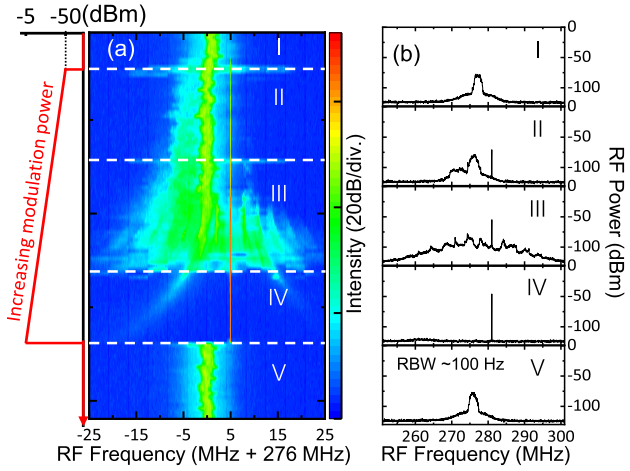


**Fig. 5.** (a) Evolution of the RF spectrum when gradually increasing the modulation power from −50 to −5 dBm. The initial breathing frequency $f_{\mathrm{br}}$ is 276 MHz (I) and the modulation frequency $f_{\mathrm{mod}}$ is 281 MHz. With the increase of the modulation power, there is a competition between $f_{\mathrm{br}}$ and $f_{\mathrm{mod}}$, and other harmonics components appear (II and III). Eventually, $f_{\mathrm{br}}$ is synchronized to $f_{\mathrm{mod}}$ as the modulation power is strong enough (IV). $f_{\mathrm{br}}$ returns back to the initial frequency after turning off the modulation signal (V). (b) Snapshots with different evolution stages in (a).

a breathing soliton state was generated at an $f_{br}$ of 276 MHz, and the linewidth of the beatnote on the RF spectrum is relatively wide (stage I). When we input the modulation signal and gradually increase the modulation power, as shown in Fig. 5(a) (stage II), a sharp peak at $f_{mod}$ appears in the RF spectrum and the intensity of the $f_{br}$ beatnote becomes weak, indicating that there exists a competition between these two frequencies and they can coexist when the modulation power is not strong enough. With further increasing the modulation power, $f_{mod}$ gradually gains the upper hand in the competition, and multiple harmonics components arising from $f_{mod}$ and $f_{br}$ can be observed in the RF spectrum, which raises the noise of the background (stage III) along with the weak $f_{br}$ beatnote. Eventually, as the modulation power is sufficiently strong, both the beatnote of $f_{br}$ and other harmonics components vanish in the RF spectrum, and only a beatnote of $f_{mod}$ with narrow linewidth exists (stage IV). According to the recorded out-of-phase oscillatory power traces of comb lines around the center and in the wings at this stage, we can confirm that the breathing soliton state still remains and $f_{br}$ is synchronized to $f_{mod}$. Finally, we turn off the modulation signal; the $f_{br}$ immediately returns to the initial $f_{br}$, and the linewidth becomes as wide as before (stage V). Since our experiment performs with a free-running pump laser without any stabilization scheme and $f_{br}$ is sensitive to the pump power and effective detuning of the pump laser, as shown in Fig. 5, the initial $f_{br}$ has obvious fluctuation and a slow red drift before disappearing in the RF spectrum. Nevertheless, once $f_{br}$ is injection locked by $f_{mod}$, even if pumped with a free-running laser, no fluctuation and drift are observed in the RF spectrum. In other words, the breathing soliton with locked frequency is robust with unstable pump conditions, and the phase noise of the system is remarkably suppressed with a much narrower linewidth of the $f_{br}$ beatnote.

### D. Control of the Breathing Frequency

Furthermore, we study the locking range of this injection-locking scheme. $f_{mod}$, which is scanned around the initial $f_{br}$ from low frequency to high frequency, is applied on the pump laser with modulation power of 0.1 mW. Figure 6(a) shows the evolution of the RF spectrum centered at 262 MHz as we slowly vary $f_{mod}$. The RF spectrum is evolved from up to down. In the beginning, when the frequency difference $\Delta f$ between $f_{mod}$ and initial $f_{br}$ is relatively large, beatnotes of initial $f_{br}$ and $f_{mod}$ and their harmonics components all exist in the RF spectrum. By continuing the scanning, when $\Delta f$ is less than ~15 MHz, the beatnotes of the initial $f_{br}$ and harmonics components are eliminated, corresponding to the injection locking of $f_{br}$. Scanning in the same direction further leads to $f_{mod}$ across the initial $f_{br}$ and out of the locking range at last. We find that after scanning out of the range, the unlocked $f_{br}$ drifts to a lower frequency of about ~5 MHz, which can be attributed to frequency red drift of the free-running pump laser during our measurement.

For the purpose of exploring the locking range as a function of modulation power, the above measurement of the locking range is repeated with varied modulation power, and the obtained results are depicted in Fig. 6(b). With the increase of the modulation power, the locking range rises rapidly at the very beginning, and then this trend tends to slow down when the modulation power is beyond 0.2 mW. In our experiment, the maximum value of modulation power allowing the existence of a breathing soliton state is 1 mW, and the corresponding locking range is 50 MHz. In the case of modulation power greater than 1 mW, the breathing soliton is annihilated. We attribute this observation to the excessively strong oscillation amplitude of the intracavity field induced by a strong modulation signal, which breaks the condition of the existence of the breathing soliton inside the microresonator. This phenomenon indicates that the modulation power has an upper limit for effective injection locking.

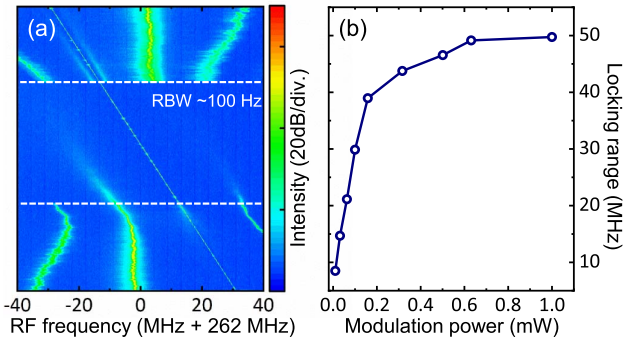


**Fig. 6.** (a) Evolution of the RF spectrum centered at 262 MHz with varied $f_{mod}$. The modulation power is 0.1 mW, and $f_{br}$ is synchronized to $f_{mod}$ when the frequency difference $\Delta f$ is less than ~15 MHz. (b) Locking ranges with varied modulation power.

## 4. CONCLUSION

In conclusion, we have experimentally demonstrated the stabilization and tuning of breathing solitons via injection locking in high-$Q$ $Si_3N_4$ microrings. By applying an appropriate external modulation signal to the pump power, the breathing frequency can be effectively locked to the modulation frequency. Both frequency fluctuation and long-term drift disappear, even with a free-running pump laser, showing the high stability of the sub-GHz breathing frequency. Besides, the linewidth of the breathing frequency beatnote also becomes obviously narrower, indicating the apparent suppression of system phase noise. Being proportional to the modulation power, the locking range is able to reach ~50 MHz in our experiment. Therefore, a tunable and stable breathing frequency can be realized by using an EOM or other kinds of modulation instruments with no need for other feedback stabilization techniques. The mechanism of injection locking is not only universal for DKS in other materials and structures, but also can be extended to stabilize oscillations in other nonlinear systems. In addition to the interesting nonlinear physics underlying the soliton and injection locking, our demonstration provides a robust way to transfer RF frequencies to broadband optical frequencies and a potential application in spectroscopy by utilizing the breathing sidebands to extract the high-order spectral information around each comb line and boost the spectral resolution.

## APPENDIX A

The CME and Lugiato–Lefever equation (LLE) are two common theoretical formalisms to simulate and describe the nonlinear dynamics inside the microresonators. The CME provides a frequency-domain description, and the LLE is a time-domain description. Either of these two formalisms can be used to equivalently describe the dynamics of Kerr frequency combs in microresonators and can be converted into each other under suitable approximations. In this work, we use the CME to perform numerical simulation. The CME provides an approach to describe the evolution of each discrete comb mode with mode index $\mu$, which is defined relative to the pump mode $\mu = 0$. The corresponding resonance frequency is $\omega_\mu = \omega_0 + D_1\mu + \frac{1}{2}D_2\mu^2 + \cdots$, where $D_1$ and $D_2$ denote the FSR and second-order dispersion (higher-order dispersion can be expressed in an analogous way). The CME of each mode is written as

$$\frac{\partial A_\mu}{\partial t} = -\frac{\kappa}{2}A_\mu + ig\sum_{k,l,n} A_k A_l^* A_n e^{-i(\omega_k-\omega_l+\omega_n-\omega_\mu)t} + \delta_{\mu 0}\sqrt{\eta\kappa}s_{\text{in}}e^{-i(\omega_p-\omega_0)t}. \tag{A1}$$

Here $A_\mu$ is the amplitude of a mode with index $\mu$ and $|A_\mu|^2$ corresponds to the number of photons in the mode. $\kappa = \kappa_0 + \kappa_{\text{ex}}$ is the loss term as a sum of the intrinsic loss $\kappa_0$ and the external loss $\kappa_{\text{ex}}$. $g = \frac{\hbar\omega_0^2 c n_2}{n_0^2 V_{\text{eff}}}$ is the nonlinear coupling coefficient, which denotes the Kerr nonlinearity with the refractive index $n_0$, nonlinear refractive index $n_2$, the effective cavity volume $V_{\text{eff}}$, and the speed of light $c$. The summation respects the relation $\mu = k + n - l$. $\delta_{\mu 0}$ is the Kronecker delta, $\eta$ is the coupling efficiency, and $s_{\text{in}} = \sqrt{P_{\text{in}}/\hbar\omega}$ is the amplitude of input power.

To remove the explicit time dependence in the nonlinear terms, by introducing $f = \sqrt{\frac{8g\eta P_{\text{in}}}{\kappa^2\hbar\omega_0}}$, $\tau = \kappa t/2$, and $a_\mu = A_\mu\sqrt{2g/\kappa}e^{-i(\omega_\mu-\omega_p-\mu D_1)t}$, we employ the following dimensionless form of the CME:

$$\frac{\partial a_\mu}{\partial \tau} = -(1 + i\Omega_\mu)a_\mu + i\sum_{k,l,n}\delta_{\mu+l-k-n}a_k a_l^* a_n + \delta_{\mu 0}f. \tag{A2}$$

Because the direct sum of nonlinear coupling is very inefficient for numerical simulation, we adopt the fast Fourier transformation (FFT) method [46]. Compared to direct calculation, the FFT allows a significant reduction of computational complexity, since the FFT complexity is $\mathcal{O}(N\log N)$ while the direct calculation is $\mathcal{O}(N^2)$ ($N$ denotes the number of modes considered in the simulation).

By introducing the operator of the Fourier transformation

$$x_\nu = \mathcal{F}[a_\mu] = \frac{1}{\sqrt{N}}\sum_\mu a_\mu e^{i2\pi\mu\nu/N}, \tag{A3}$$

and the inverse Fourier transformation

$$a_\mu = \mathcal{F}^{-1}[x_\nu] = \frac{1}{\sqrt{N}}\sum_\nu x_\nu e^{-i2\pi\mu\nu/N}, \tag{A4}$$

the CME is as follows:

$$\frac{\partial a_\mu}{\partial \tau} = -(1 + i\Omega_\mu)a_\mu + i\mathcal{F}^{-1}[|\mathcal{F}[\vec{a}]|^2\mathcal{F}[\vec{a}]]_\mu + \delta_{\mu 0}f. \tag{A5}$$

Here $\vec{a} = (a_{-N}, a_{-N-1}, \ldots 0, \ldots, a_N)$ and $\mathcal{F}$ is Fourier transformation.

For specificity, we use parameters similar to our $Si_3N_4$ microring resonator with a 800 nm × 1800 nm cross section and a 100 μm radius, that is, $\lambda_0 = 1570$ nm, $\kappa_0 = \frac{\omega_0}{Q_0}$, $Q_0 = 3\times10^6$, $\eta = 0.5$, $D_1 = 2\pi\times230$ GHz, $D_2 = 2\pi\times6$ MHz, $g \approx 2.98$, $P_{\text{in}} = 100$ mW, and the number of modes $N = 121$. In order to map the evolution of the intracavity power, we fix the input power and increase the detuning. Four intracavity state, including a primary comb state, a modulation instability comb state, a breathing soliton state, and a stationary soliton state, can be identified.

For simulation of the breathing soliton state, we fix the input power and the detuning to make the intracavity power stay at the breathing soliton stage. Then an amplitude modulation is applied to the driving item $f$. The expression of the modulated driving item $f'$ is written as

$$f' = \frac{f}{i-1}\left\{e^{i\left[\frac{\pi}{2}+\pi\epsilon\,\sin(2\pi\nu t)\right]} - 1\right\}, \tag{A6}$$

$$= \frac{f}{i-1}[ie^{i\pi\epsilon\,\sin(2\pi\nu t)} - i + i - 1], \tag{A7}$$

$$= f + \frac{if}{i-1}[e^{i\pi\epsilon\,\sin(2\pi\nu t)} - 1]. \tag{A8}$$

The $|f'|^2$ is as follows:

$$|f'|^2 = |f|^2\left|1 - \frac{i-1}{2}[e^{i\pi\epsilon\,\sin(2\pi\nu t)} - 1]\right|^2, \tag{A9}$$

$$= |f|^2\{\sin[\pi\epsilon\,\sin(2\pi\nu t)] + \cos[\pi\epsilon\,\sin(2\pi\nu t)]\}, \tag{A10}$$

$$= |f|^2\sqrt{2}\cos\left[\pi\epsilon\,\sin(2\pi\nu t) - \frac{\pi}{4}\right]. \tag{A11}$$

Here $\epsilon$ is the modulation depth and $\nu$ is the modulation frequency. In our simulation, the initial breathing frequency is 287 MHz, the modulation frequency is 270 MHz, and the modulation depth is $\epsilon = 0.01$.

In order to broaden the laser linewidth and make the simulation more realistic, a noise noise($t$) is added to the driving item as

$$f = E_{\text{in}} \times [1 + \text{noise}(t)]. \tag{A12}$$

Noise($t$) is a complex number that contains the amplitude and phase of the noise. In the frequency domain, the spectrum of the noise is described by $S(\nu) = \frac{(1+a\times R_1)\times e^{i2\pi R_2}}{(\nu/10^4)^b}$. $R_1$, $R_2 \in [0, 1]$ are the random numbers. $a$, $b$ are the amplitude of the fluctuation and the power of frequency $\nu$. In simulation, $a = 0.1$ and $b = 0.2$ are suitable. In the time domain, the maximum of |noise($t$)| is about 2%.

From our simulation, if the modulation signal is too weak, the initial breathing frequency will remain and a harmonic signal will be generated. Meanwhile, if the modulation signal is too strong, the oscillation of the pump power will break the intracavity field and only the CW background leaves. When the modulation frequency is close enough to the breathing frequency and the modulation depth is proper, simulation results show that the breathing frequency can be injection locked to the modulation frequency, and the linewidth of the RF spectrum becomes much narrower, meaning that the phase noise of the system has been suppressed effectively. Our numerical simulation exhibits a good agreement with experimental results.

**Funding.** National Key Research and Development Program of China (2016YFA0301303); National Natural Science Foundation of China (11722436, 11934012); Anhui Initiative in Quantum Information Technologies (AHY130200); Fundamental Research Funds for the Central Universities.

**Acknowledgment.** This work was partially carried out at the USTC Center for Micro and Nanoscale Research and Fabrication.

**Disclosures.** The authors declare no conflicts of interest.

[†]These authors contributed equally to this paper.

## REFERENCES

1. T. J. Kippenberg, A. L. Gaeta, M. Lipson, and M. L. Gorodetsky, "Dissipative Kerr solitons in optical microresonators," Science **361**, eaan8083 (2018).
2. N. Akhmediev and A. Ankiewicz, *Dissipative Solitons: From Optics to Biology and Medicine* (Springer, 2008).
3. S. Wabnitz, "Suppression of interactions in a phase-locked soliton optical memory," Opt. Lett. **18**, 601–603 (1993).
4. F. Leo, S. Coen, P. Kockaert, S.-P. Gorza, P. Emplit, and M. Haelterman, "Temporal cavity solitons in one-dimensional Kerr media as bits in an all-optical buffer," Nat. Photonics **4**, 471–476 (2010).
5. X. Yi, Q.-F. Yang, K. Y. Yang, M.-G. Suh, and K. Vahala, "Soliton frequency comb at microwave rates in a high-*Q* silica microresonator," Optica **2**, 1078–1085 (2015).
6. V. Brasch, M. Geiselmann, T. Herr, G. Lihachev, M. H. Pfeiffer, M. L. Gorodetsky, and T. J. Kippenberg, "Photonic chip-based optical frequency comb using soliton Cherenkov radiation," Science **351**, 357–360 (2016).
7. X. Xue, X. Zheng, and B. Zhou, "Super-efficient temporal solitons in mutually coupled optical cavities," Nat. Photonics **13**, 616–622 (2019).
8. J. Peng, S. Boscolo, Z. Zhao, and H. Zeng, "Breathing dissipative solitons in mode-locked fiber lasers," Sci. Adv. **5**, eaax1110 (2019).
9. K. J. Vahala, "Optical microcavities," Nature **424**, 839–846 (2003).
10. T. Herr, V. Brasch, J. D. Jost, C. Y. Wang, N. M. Kondratiev, M. L. Gorodetsky, and T. J. Kippenberg, "Temporal solitons in optical microresonators," Nat. Photonics **8**, 145–152 (2014).
11. H. Zhou, Y. Geng, W. Cui, S.-W. Huang, Q. Zhou, K. Qiu, and C. W. Wong, "Soliton bursts and deterministic dissipative Kerr soliton generation in auxiliary-assisted microcavities," Light Sci. Appl. **8**, 1 (2019).
12. H.-J. Chen, Q.-X. Ji, H. Wang, Q.-F. Yang, Q.-T. Cao, Q. Gong, X. Yi, and Y.-F. Xiao, "Chaos-assisted two-octave-spanning microcombs," Nat. Commun. **11**, 2336 (2020).
13. W. Wang, W. Zhang, Z. Lu, S. T. Chu, B. E. Little, Q. Yang, L. Wang, and W. Zhao, "Self-locked orthogonal polarized dual comb in a microresonator," Photon. Res. **6**, 363–367 (2018).
14. X. Xu, J. Wu, T. G. Nguyen, T. Moein, S. T. Chu, B. E. Little, R. Morandotti, A. Mitchell, and D. J. Moss, "Photonic microwave true time delays for phased array antennas using a 49 GHz FSR integrated optical micro-comb source invited," Photon. Res. **6**, B30–B36 (2018).
15. J. Ma, L. Xiao, J. Gu, H. Li, X. Cheng, G. He, X. Jiang, and M. Xiao, "Visible Kerr comb generation in a high-Q silica microdisk resonator with a large wedge angle," Photon. Res. **7**, 573–578 (2019).
16. P. Del'Haye, A. Schliesser, O. Arcizet, T. Wilken, R. Holzwarth, and T. J. Kippenberg, "Optical frequency comb generation from a monolithic microresonator," Nature **450**, 1214–1217 (2007).
17. P. Grelu and N. Akhmediev, "Dissipative solitons for mode-locked lasers," Nat. Photonics **6**, 84–92 (2012).
18. P. Marin-Palomo, J. N. Kemal, M. Karpov, A. Kordts, J. Pfeifle, M. H. Pfeiffer, P. Trocha, S. Wolf, V. Brasch, M. H. Anderson, R. Rosenberger, K. Vijayan, W. Freude, T. J. Kippenberg, and C. Koos, "Microresonator-based solitons for massively parallel coherent optical communications," Nature **546**, 274–279 (2017).
19. F.-X. Wang, W. Wang, R. Niu, X. Wang, C.-L. Zou, C.-H. Dong, B. E. Little, S. T. Chu, H. Liu, P. Hao, S. Liu, S. Wang, Z.-Q. Yin, D.-Y. He, W. Zhang, W. Zhao, Z.-F. Han, G.-C. Guo, and W. Chen, "Quantum key distribution with on-chip dissipative Kerr soliton," Laser Photon. Rev. **14**, 1900190 (2020).
20. M.-G. Suh and K. J. Vahala, "Soliton microcomb range measurement," Science **359**, 884–887 (2018).
21. P. Trocha, M. Karpov, D. Ganin, M. H. P. Pfeiffer, A. Kordts, S. Wolf, J. Krockenberger, P. Marin-Palomo, C. Weimann, S. Randel, W. Freude, T. J. Kippenberg, and C. Koos, "Ultrafast optical ranging using microresonator soliton frequency combs," Science **359**, 887–891 (2018).
22. M.-G. Suh, Q.-F. Yang, K. Y. Yang, X. Yi, and K. J. Vahala, "Microresonator soliton dual-comb spectroscopy," Science **354**, 600–603 (2016).
23. A. Dutt, C. Joshi, X. Ji, J. Cardenas, Y. Okawachi, K. Luke, A. L. Gaeta, and M. Lipson, "On-chip dual-comb source for spectroscopy," Sci. Adv. **4**, e1701858 (2018).
24. W. Liang, D. Eliyahu, V. S. Ilchenko, A. A. Savchenkov, A. B. Matsko, D. Seidel, and L. Maleki, "High spectral purity Kerr frequency comb radio frequency photonic oscillator," Nat. Commun. **6**, 7957 (2015).
25. W. Weng, E. Lucas, G. Lihachev, V. E. Lobanov, H. Guo, M. L. Gorodetsky, and T. J. Kippenberg, "Spectral purification of microwave signals with disciplined dissipative Kerr solitons," Phys. Rev. Lett. **122**, 013902 (2019).
26. Z. L. Newman, V. Maurice, T. Drake, J. R. Stone, T. C. Briles, D. T. Spencer, C. Fredrick, Q. Li, D. Westly, B. R. Ilic, B. Shen, M.-G. Suh, K. Y. Yang, C. Johnson, D. M. S. Johnson, L. Hollberg, K. J. Vahala, K. Srinivasan, S. A. Diddams, J. Kitching, S. B. Papp, and M. T. Hummon, "Architecture for the photonic integration of an optical atomic clock," Optica **6**, 680–685 (2019).
27. M.-G. Suh, X. Yi, Y.-H. Lai, S. Leifer, I. S. Grudinin, G. Vasisht, E. C. Martin, M. P. Fitzgerald, G. Doppmann, J. Wang, D. Mawet, S. B. Papp, S. A. Diddams, C. Beichman, and K. Vahala, "Searching for exoplanets using a microresonator astrocomb," Nat. Photonics **13**, 25–30 (2019).
28. E. Obrzud, M. Rainer, A. Harutyunyan, M. H. Anderson, J. Liu, M. Geiselmann, B. Chazelas, S. Kundermann, S. Lecomte, M. Cecconi, A. Ghedina, E. Molinari, F. Pepe, F. Wildi, F. Bouchy, T. J. Kippenberg, and T. Herr, "A microphotonic astrocomb," Nat. Photonics **13**, 31–35 (2019).
29. X. Xue, Y. Xuan, Y. Liu, P. H. Wang, S. Chen, J. Wang, D. E. Leaird, M. Qi, and A. M. Weiner, "Mode-locked dark pulse Kerr combs in normal-dispersion microresonators," Nat. Photonics **9**, 594–600 (2015).
30. M. Karpov, H. Guo, A. Kordts, V. Brasch, M. H. P. Pfeiffer, M. Zervas, M. Geiselmann, and T. J. Kippenberg, "Raman self-frequency shift of dissipative Kerr solitons in an optical microresonator," Phys. Rev. Lett. **116**, 103902 (2016).
31. C. Bao, J. A. Jaramillo-Villegas, Y. Xuan, D. E. Leaird, M. Qi, and A. M. Weiner, "Observation of Fermi-Pasta-Ulam recurrence induced by breather solitons in an optical microresonator," Phys. Rev. Lett. **117**, 163901 (2016).
32. M. Yu, J. K. Jang, Y. Okawachi, A. G. Griffith, K. Luke, S. A. Miller, X. Ji, M. Lipson, and A. L. Gaeta, "Breather soliton dynamics in microresonators," Nat. Commun. **8**, 145969 (2017).

33. E. Lucas, M. Karpov, H. Guo, M. Gorodetsky, and T. J. Kippenberg, "Breathing dissipative solitons in optical microresonators," Nat. Commun. **8**, 736 (2017).
34. X. Yi, Q.-F. Yang, K. Y. Yang, and K. Vahala, "Imaging soliton dynamics in optical microcavities," Nat. Commun. **9**, 3565 (2018).
35. E. Lucas, G. Lihachev, R. Bouchand, N. G. Pavlov, A. S. Raja, M. Karpov, M. L. Gorodetsky, and T. J. Kippenberg, "Spatial multiplexing of soliton microcombs," Nat. Photonics **12**, 699–705 (2018).
36. H. Guo, E. Lucas, M. H. Pfeiffer, M. Karpov, M. Anderson, J. Liu, M. Geiselmann, J. D. Jost, and T. J. Kippenberg, "Intermode breather solitons in optical microresonators," Phys. Rev. X **7**, 041055 (2017).
37. C. Bao, Y. Xuan, C. Wang, A. Fülöp, D. E. Leaird, M. Qi, and A. M. Weiner, "Observation of breathing dark pulses in normal dispersion optical microresonators," Phys. Rev. Lett. **121**, 257401 (2018).
38. D. C. Cole and S. B. Papp, "Subharmonic entrainment of Kerr breather solitons," Phys. Rev. Lett. **123**, 173904 (2019).
39. P. Liao, K. Zou, C. Bao, A. Kordts, M. Karpov, M. H. P. Pfeiffer, L. Zhang, Y. Cao, A. Almaiman, F. Alishashi, A. Mohajerin-Ariaei, A. Fallahpour, M. Tur, T. J. Kippenberg, and A. E. Willner, "Chip-scale dual-comb source using a breathing soliton with an increased resolution," in *Conference on Lasers and Electro-Optics* (Optical Society of America, 2018), paper JTh5A.4.
40. K. Luke, A. Dutt, C. B. Poitras, and M. Lipson, "Overcoming $Si_3N_4$ film stress limitations for high quality factor ring resonators," Opt. Express **21**, 22829–22833 (2013).
41. M. H. Pfeiffer, A. Kordts, V. Brasch, M. Zervas, M. Geiselmann, J. D. Jost, and T. J. Kippenberg, "Photonic damascene process for integrated high-*Q* microresonator based nonlinear photonics," Optica **3**, 20–25 (2016).
42. Y. Xuan, Y. Liu, L. T. Varghese, A. J. Metcalf, X. Xue, P.-H. Wang, K. Han, J. A. Jaramillo-Villegas, A. Al Noman, C. Wang, S. Kim, M. Teng, Y. J. Lee, B. Niu, L. Fan, J. Wang, D. E. Leaird, A. M. Weiner, and M. Qi, "High-*Q* silicon nitride microresonators exhibiting low-power frequency comb initiation," Optica **3**, 1171–1180 (2016).
43. K. Luke, Y. Okawachi, M. R. Lamont, A. L. Gaeta, and M. Lipson, "Broadband mid-infrared frequency comb generation in a $Si_3N_4$ microresonator," Opt. Lett. **40**, 4823–4826 (2015).
44. M. H. Pfeiffer, C. Herkommer, L. Jumqiu, T. Morais, M. Zervas, M. Geiselmann, and T. Kippenberg, "Photonic damascene process for low-loss, high-confinement silicon nitride waveguides," IEEE J. Sel. Top. Quantum Electron. **24**, 6101411 (2018).
45. Y. K. Chembo and N. Yu, "Modal expansion approach to optical-frequency-comb generation with monolithic whispering-gallery-mode resonators," Phys. Rev. A **82**, 033801 (2010).
46. T. Hansson, D. Modotto, and S. Wabnitz, "On the numerical simulation of Kerr frequency combs using coupled mode equations," Opt. Commun. **312**, 134–136 (2014).
47. X. Guo, C.-L. Zou, H. Jung, Z. Gong, A. Bruch, L. Jiang, and H. X. Tang, "Efficient generation of a near-visible frequency comb via Cherenkov-like radiation from a Kerr microcomb," Phys. Rev. Appl. **10**, 014012 (2018).